DRAFT VERSION JANUARY 23, 2017
Preprint typeset using LaTeX style emulateapj v. 04/17/13

arXiv:1701.05624v1 [astro-ph.GA] 19 Jan 2017

THE VULTURE SURVEY I: ANALYZING THE EVOLUTION OF Mg II ABSORBERS

NIGEL L. MATHES[1], CHRISTOPHER W. CHURCHILL[1], AND MICHAEL T. MURPHY[2]

Draft version January 23, 2017

ABSTRACT

We present detailed measurements of the redshift path density, equivalent width distribution, column density distribution, and redshift evolution of Mg II absorbers as measured in archival spectra from the UVES spectrograph at the Very Large Telescope (VLT/UVES) and the HIRES spectrograph at the Keck Telescope (Keck/HIRES) to equivalent width detection limits below 0.01 Å. This survey examines 432 VLT/UVES spectra from the UVES SQUAD collaboration and 170 Keck/HIRES spectra from the KODIAQ group, allowing for detections of intervening Mg II absorbers spanning redshifts $0.1 < z < 2.6$. We employ an accurate, automated approach to line detection which consistently detects redshifted absorption lines. We measure the equivalent widths, apparent optical depth column densities, and velocity widths for each absorbing system. Using our complete sample of all detectable Mg II absorbers, we can accurately determine the redshift path density of absorbers across cosmic time. We measure evolution in the comoving Mg II line density, dN/dX, finding more high equivalent width absorbers at $z = 2$ than at present. We also measure evolution in the equivalent width distribution, parameterized by a Schechter function fit, finding a shallower weak-end slope (α) for absorbers at redshifts between $1.53 < z < 2.64$, with $\alpha = -0.81 \pm 0.12$, compared to absorbers between $0.14 < z < 0.78$, where $\alpha = -1.09 \pm 0.09$. Finally, we calculate the cosmic mass fraction of Mg II using the column density distribution, finding that $\Omega_{\rm Mg\,II}$ increases from $\Omega_{\rm Mg\,II} = (0.9 \pm 0.2) \times 10^{-8}$ at $< z > = 0.49$ to $\Omega_{\rm Mg\,II} = (1.4 \pm 0.2) \times 10^{-8}$ at $< z > = 2.1$. We find that weak Mg II absorbers, those with equivalent widths less than 0.3 Å, are physically distinct and evolve separately from very strong Mg II absorbers, which have equivalent widths greater than 1.0 Å. We compare our observed evolutionary trends in the distributions of Mg II absorbers to previously studied cosmic trends in metallicty, the ionizing ultraviolet background, and star formation in order to conclude that galaxies eject more metal enriched gas into their halos around $z = 2$ than at lower redshifts in the form of high equivalent width Mg II-absorbing outflows. Over time from $z = 2$ to the present, these feedback processes decline and the evolving conditions in the circumgalactic medium give rise to a population of low equivalent width, passive Mg II absorbers.

Keywords: galaxies: halos — quasars: absorption lines

1. INTRODUCTION

One of the most important questions in modern studies of galactic evolution asks, how do baryons cycle into and out of galaxies, and how does this cycle determine the growth and evolution of galaxies themselves? More specifically, how does the process of gas accretion, star formation, and subsequent supernovae-driven feedback shape both the galaxies themselves and their circumgalactic medium (CGM)? By using spectroscopic observations of quasars, we can identify and analyze metal line absorbers in and around the halos of foreground galaxies. Though absorption line studies by themselves cannot directly answer these questions, the statistical results from such studies can provide vital information from which further progress can be made.

One of the most prolific absorption features, the Mg II $\lambda\lambda 2796, 2803$ doublet, traces cool ($T \simeq 10^4$ K; Churchill et al. (2003)) metal enriched gas in the disks and halos of galaxies. It is one of the best tracers of this gas because it can exist in a wide range of ionizing conditions, ranging in ionization parameter from $-5 < \log U < 1$ (Churchill et al. 1999), it is observable in optical wavelengths for redshifts between $0.1 < z < 2.6$, and it has predictable line characteristics defined by its resonant doublet nature which make it ideal for automated searches.

The origin of Mg II absorbing gas is still debated. As summarized in Kacprzak et al. (2011) and Matejek et al. (2013), two separate interpretations exist to explain the origin of strong, high equivalent width (W_r) Mg II absorbers ($W_r^{\lambda 2796} > 0.3$ Å) and weak, low equivalent width ($W_r^{\lambda 2796} < 0.3$ Å) Mg II absorbers. For the strong, higher equivalent width systems, multiple correlations exist between the rest frame Mg II equivalent width around galaxies and the host galaxy's star formation properties. Zibetti et al. (2007), Lundgren et al. (2009), Noterdaeme et al. (2010), Bordoloi et al. (2011), and Nestor et al. (2011) all found a correlation betwen $W_r^{\lambda 2796}$ and blue host galaxy color, showing that galaxies with more active star formation have more metal enriched gas in their halos. Bordoloi et al. (2014) also found that Mg II equivalent width increases with increasing star formation rate density. In addition, spectroscopic observations of star forming galaxies have revealed strong Mg II absorption blueshifted $300 - 1000$ km s^{-1} relative to the host galaxy (Tremonti et al. 2007; Weiner et al. 2009; Martin & Bouché 2009; Rubin et al. 2010). Bouché et al. (2006) found an anti-correlation between galaxy halo mass, derived from the cross-correlation between Mg II absorption systems and luminous red galaxies, and Mg II equivalent width, showing that individual clouds of a Mg II system are not virialized in the halos of galaxies. They interpreted their results as a strong indication that high equivalent width absorbers with $W_r^{\lambda 2796} \gtrsim 2$ Å arise in

[1] New Mexico State University, Las Cruces, NM 88003, United States
[2] Centre for Astrophysics and Supercomputing, Swinburne University of Technology, Victoria 3122, Australia

galactic outflows. Marginal anti-correlations between Mg II equivalent width and galaxy halo mass using the same cross-correlation method were also reported by Gauthier et al. (2009) and Lundgren et al. (2009). It is imporant to note, however, that Churchill et al. (2013a) and Churchill et al. (2013b) find no correlation between $W_r^{\lambda 2796}$ and halo mass when halo mass is derived from abundance matching. They instead find that galaxies inhabiting more massive dark matter halos have stronger absorption at a given distance.

For the weak, lower equivalent width systems, it seems none of the above correlations hold. Chen et al. (2010), Kacprzak et al. (2011), and Lovegrove & Simcoe (2011) found little evidence for a correlation between galaxy color and Mg II equivalent width when restricting their samples to weak absorbers. Kacprzak et al. (2011) measured the orientation of galaxies relative to Mg II detections in the sight lines of background quasars and identified low metallicity, low equivalent width Mg II absorbers co-planar with some some galaxy disks, implying structures associated with accreting filaments as opposed to outflows, which are more often observed perpendicular to the galaxy disk (Bordoloi et al. 2011; Kacprzak et al. 2012). Finally, the simulations of Stewart et al. (2011) and Ford et al. (2013) revealed a reservoir of low-ionization, metal enriched, co-rotating gas around massive galaxies. Together, these studies imply that weak Mg II absorption systems may preferentially trace low metallicity infall and co-rotating gas in the circumgalactic medium.

Nielsen et al. (2013b) constructed a sample of Mg II absorbers and their associated galaxies and examined both strong and weak Mg II absorbers from $0.07 \leq z \leq 1.1$. In the subsequent analysis of their sample, Nielsen et al. (2013a) found a more extended Mg II absorbing CGM around higher luminosity, bluer, higher redshift galaxies. In addition, in Nielsen et al. (2016), they found that bluer galaxies replenish their Mg II absorbing CGM through outflows, whereas red galaxies do not. Finally, in Nielsen et al. (2015), it is made clear that the largest velocity dispersions in Mg II absorbing systems are measured around blue, face-on galaxies probed along their minor axis, strongly suggesting that these Mg II absorbers originate in bi-conical outflows.

Many surveys have been undertaken to inventory Mg II absorbers and examine their evolution. The earliest studies (Lanzetta et al. 1987; Tytler et al. 1987; Sargent et al. 1988; Steidel & Sargent 1992) found that Mg II systems with rest equivalent widths above 0.3 Å show no evolution in dN/dz between redshifts $0.2 < z < 2.15$. These studies also found that the equivalent width distribution function, $f(W_r^{\lambda 2796})$, could be fit equally well with either an exponential or a power-law function. It remains uncertain whether the cosmic distribution of Mg II in galactic halos exhibits a fractal, self-similar nature, or if $f(W_r^{\lambda 2796})$ flattens at equivalent widths below $W_r^{\lambda 2796} < 0.3$ Å.

Mg II absorption surveys have taken one of two different approaches to try to analyze the global distribution of Mg II absorbing gas across cosmic time. Churchill et al. (1999) and Narayanan et al. (2007) aimed to determine more precisely how dN/dz and $f(W_r^{\lambda 2796})$ evolve with redshift by surveying weak Mg II absorbers. They found that, for these low equivalent width absorbers, dN/dz increases as a function of increasing redshift up until $z = 1.4$. At higher redshifts, dN/dz falls to lower values, though the uncertainties are large. In addition, they found the equivalent width distribution function for weak absorbers is best fit by a power-law, strongly disfavoring an exponential fit to the overall distribution.

The most recent studies have employed new multi-object spectrographs such as the Sloan Digital Sky Survey (SDSS) and the FIRE spectrograph on the Magellan Baade Telescope (Nestor et al. 2005; Matejek & Simcoe 2012; Chen et al. 2016). Nestor et al. (2005), who examined over 1300 intervening Mg II absorbers in SDSS quasar spectra with $W_r^{\lambda 2796} > 0.3$ Å, found that the equivalent width distribution function is well fit by an exponential. They did not find evidence for redshift evolution in systems with $0.4 < W_r^{\lambda 2796} < 2$ Å, but observed an enhancement in the number of $W_r^{\lambda 2796} > 2$ Å absorbers per comoving redshift path length as a function of increasing redshift from $z \sim 0$ up to $z \sim 2$. Matejek & Simcoe (2012) and Chen et al. (2016), analyzing 279 Mg II absorbing systems from $2 < z < 7$ in infrared FIRE spectra, also found that the equivalent width distribution function is well fit by an exponential. They also observed that systems with $W_r^{\lambda 2796} < 1.0$ Å show no evolution with redshift, but higher equivalent width systems grow in number density from low redshift to $z \sim 3$, after which the number density declines. Collectively, these surveys imply physical changes in the astrophysical processes or in the state of the gas structures in the environments giving rise to Mg II absorption as the universe ages.

The properties of a given Mg II absorbing cloud are governed by the total amount of gas present, the gas phase metallicity, and the nature of the background radiation incident on the cloud. As shown by Quiret et al. (2016), studying a large sample of damped Lyα absorbers (DLAs; neutral hydrogen absorbers with $\log(N(\mathrm{HI})) > 20.3$) and sub-DLAs ($19.0\ \mathrm{cm}^{-2} < \log(N(\mathrm{HI})) < 20.3\ \mathrm{cm}^{-2}$), the average metallicity of the circumgalactic medium decreases from $z = 0$ to $z = 5$. In addition, Ménard & Chelouche (2009) show that a correlation exists between the neutral hydrogen column density of an absorber and the rest frame Mg II equivalent width, with stronger Mg II absorbing systems having large H I column densities. As Mg II absorbers are often found associated with nearby galaxies, one can expect that the metallicity evolution of DLAs and sub-DLAs should be reflected in the evolution of Mg II absorbing systems (Kulkarni & Fall 2002; Prochaska et al. 2003; Kulkarni et al. 2005, 2007).

The cosmic ionizing background also changes dramatically from $z = 0$ to $z = 2.5$. Haardt & Madau (2012) showed that the slope and intensity of the diffuse UV/X-ray ionizing background increase as redshift increases, with a harder, more intense ionizing background present at higher redshift. Specifically, the comoving 1 Rydberg emissivity increases from $\sim 2 \times 10^{23}$ erg s^{-1} Mpc^{-3} Hz^{-1} at $z = 0$ to $\sim 70 \times 10^{23}$ erg s^{-1} Mpc^{-3} Hz^{-1} at $z = 2.5$. Mg II absorbers are subject primarily to this UV background, with very little contribution from stellar radiation from a nearby galaxy (Churchill et al. 1999; Charlton et al. 2000; Rigby et al. 2002).

Behroozi et al. (2013) showed that the cosmic star formation rate peaks around $z \sim 2$. At this point in time, galaxies are on average forming stars at a rate ten times greater than at $z = 0$. In conjunction with the fact that galactic-scale outflows can be driven by star formation (Zhu et al. 2015), and these outflows can eject Mg II absorbing gas to large galactocentric radii (Sharma & Nath 2013; Kacprzak et al. 2012; Nestor et al. 2011), it follows that more metal enriched gas, traced by Mg II absorbers, should be driven out of galaxies at $z \sim 2$. One goal of The Vulture Survey is to find and analyze definitive observational signatures of this energetic epoch.

We now aim to better understand the complex relationship between absorbing gas in the CGM/IGM and the physical processes shaping galaxy formation as the universe ages. For our survey, we will analyze the largest, most comprehensive sample of high resolution, high S/N quasar spectra to uniformly observe both strong and weak Mg II absorbers. We hope to finally bridge the equivalent width dichotomy in prior Mg II absorption line surveys by analyzing large numbers of both strong and weak absorbers. To do so, we will examine quasar spectra observed with either the VLT/UVES (Dekker et al. 2000) or Keck/HIRES (Vogt et al. 1994) spectrographs. We aim to characterize the evolution in the number density of all Mg II absorbers from present to beyond the peak of the cosmic star formation rate. We interpret these results in the context of global evolution in metallicity around galaxies, the ionizing background, and cosmic star formation.

We begin by explaining the methods of acquiring and analyzing the quasar spectra in Section 2. In Section 3, we present the results showing the evolution of the Mg II equivalent width distribution, dN/dX, and the Mg II column density distribution across redshift. We also analyze the functional fit to both the equivalent width and column density distributions. In Section 4 we discuss the redshift evolution of all types of Mg II absorbers and derive the relative matter density contributed to the universe by Mg II, $\Omega_{\rm Mg\,II}$. In Section 5 we summarize our results and look to future studies using this rich data set, including a companion analysis of intervening C IV absorbers and detailed kinematic analysis of intervening absorbing systems. For all calculations, we adopt the most recently published Planck cosmology, with $H_0 = 67.81$ km s^{-1} Mpc, $\Omega_M = 0.308$, and $\Omega_\Lambda = 0.692$ (Planck Collaboration et al. 2016).

2. DATA AND ANALYSIS

2.1. *Quasar Spectra Sample*

We have assembled a sample of 602 archival quasar spectra observed with the VLT/UVES and Keck/HIRES spectrographs. The data originate from two archival data mining efforts - the UVES SQUAD collaboration (432 spectra) led by Michael Murphy, and the KODIAQ Survey (170 spectra) led by John O'Meara (O'Meara et al. 2015). The spectra range in signal-to-noise ratio (S/N) from 4 to 288 per $1.3-2.5$ km s^{-1} pixel, with the pixel size dependent upon the resolution of the spectrum. The mean S/N for the sample is 38 per pixel. Quasar emission redshifts span $0.014 < z < 5.292$. Wavelength coverage for each spectrum varies based upon the settings used for each spectrograph. VLT/UVES has 3 CCD chips available, offering large wavelength coverage from ~ 3000 to $\sim 10\,000$ Å. However, wavelength coverage available for each quasar spectum varies based upon the selected cross-disperser settings. The exposures used from Keck/HIRES were taken from 2004 to present, when a 3 chip CCD mosiac was installed, also allowing wavelength coverage from ~ 3000 to $\sim 10\,000$ Å. Again, though, individual quasar observations vary in wavelength coverage based upon cross-disperser angle. We detect 1180 Mg II absorbing systems from $0.14 < z < 2.64$ to a detection limit of $W_r^{\lambda 2796} \simeq 0.01$ Å for regions with $S/N > 40$ per pixel.

The archival quasar spectra used to construct The Vulture Survey were observed for a multitude of reasons. In cases where observations were taken to target a previously known absorption line system, these detections could bias our sample when calculating dN/dz and dN/dX. Because early studies which discovered Mg II absorbers did not have the sensitivity to detect weak, low equivalent width systems, quasar spectra were never selected based upon the presence of weak absorption. However, some spectra were selected based on the presence of strong, $W_r^{\lambda 2796} > 0.3$ Å systems. In order to properly quantify any bias, we compare our work to the massive, unbiased sample of the Sloan Digital Sky Survey (SDSS). Specifically, we turn to the work of Nestor et al. (2005) who inventoried strong Mg II absorbers in SDSS quasar spectra. In Nestor et al. (2005), the authors constructed the equivalent width frequency distribution for absorbers with $W_r^{\lambda 2796} > 0.3$ Å and found the best fit to this distribution was an exponential function of the form,

$$f(W_r^{\lambda 2796}) = \frac{N^*}{W^*} e^{-(W_r^{\lambda 2796}/W^*)} \quad (1)$$

where N^* and W^* are constants. In order to compare to the SDSS data, we limit our sample to absorbers with equivalent widths $W_r^{\lambda 2796} > 0.3$ Å and calculate the equivalent width frequency distribution. In Figure 1(a), we show $f(W_r^{\lambda 2796})$ for The Vulture Survey and an exponential fit to our data, along with the exponential fit of Nestor et al. (2005). Nestor et al. (2005) found the best-fit parameters and corresponding 1σ uncertainties to be $N^* = 1.187 \pm 0.052$ and $W^* = 0.702 \pm 0.017$. When we perform the same analysis, fitting Equation 1 to The Vulture Survey data, we derive $N^* = 1.39 \pm 0.10$ and $W^* = 0.74 \pm 0.05$. By eye, there appears a slight excess in the number of Mg II absorbers above $W_r^{\lambda 2796} > 3$ Å.

In order to statistically determine the bias in our sample, we perform a Kolmogorov–Smirnov (KS) test to quantitatively measure the similarity between our sample of absorbers with $W_r^{\lambda 2796} > 0.3$ Å and the SDSS sample of Nestor et al. (2005). We first sample a population of 1331 measured absorber equivalent widths, matching the SDSS sample size, from the exponential fit to the equivalent width ditribution of Nestor et al. (2005), incorporating the reported 1σ scatter in the fit parameters. This allows us to directly compare to the sample of measured Mg II equivalent widths from The Vulture Survey. In Figure 1(b), we show the cumulative distribution of the strong absorbers in The Vulture Survey in black, along with the exponential fit to our data and the fit of Nestor et al. (2005). We then perform a two-sample KS test, calculating the P-value, which is the probability that the two samples are drawn from different underlying distributions, defined as P(K-S). To avoid issues due to the random resampling of the Nestor et al. (2005) distribution, we repeat this exercise one million times as a Monte-Carlo method, generating an ensemble of P(K-S) values. We take the mean P(K-S) value as the true probability that the samples are inconsistent, and the standard deviation about this mean as the 1σ uncertainty. Our criterion to assert that our sample is not inconsistent with an unbiased sample requires P(K-S)> 0.0027, which means that it could not be ruled out at the 3σ level that the two populations are consistent with one another. With P(K-S)$= 0.112 \pm 0.049$, and only one instance out of the million Monte-Carlo runs exhibiting a P(K-S) value below 0.0027, we conclude that our sample is not inconsistent with an unbiased sample, even at the 2σ level, and that the strong absorbers in The Vulture Survey could very well have originated from the same underlying population as the unbiased SDSS quasar spectra sample.

2.2. *Data Reduction and Line Detection*

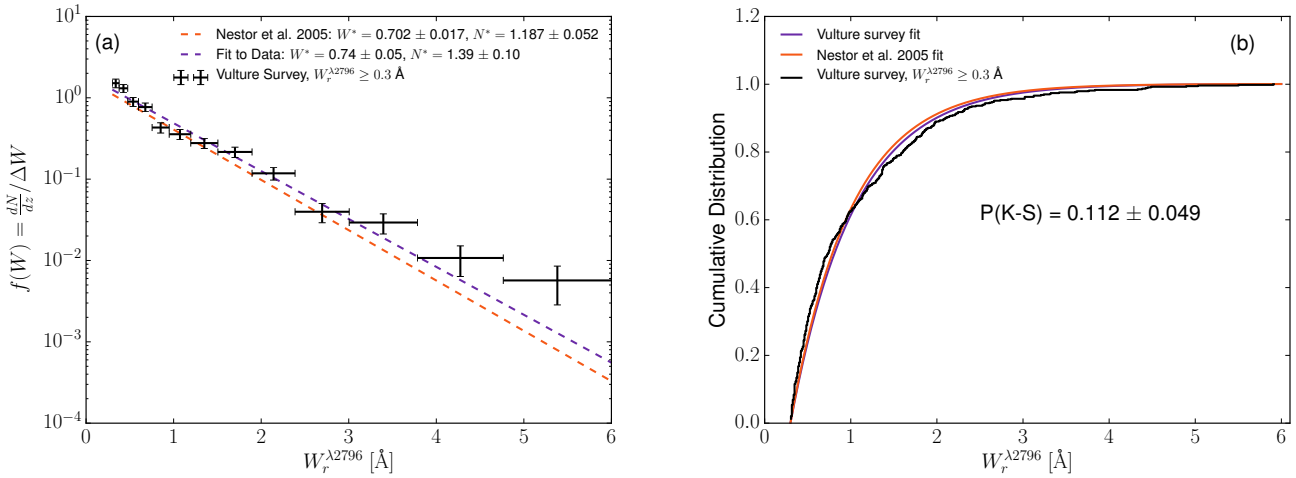
(a)
Nestor et al. 2005: $W^* = 0.702 \pm 0.017$, $N^* = 1.187 \pm 0.052$
Fit to Data: $W^* = 0.74 \pm 0.05$, $N^* = 1.39 \pm 0.10$
Vulture Survey, $W_r^{\lambda 2796} \geq 0.3$ Å
$f(W) = \frac{dN}{dz}/\Delta W$
$W_r^{\lambda 2796}$ [Å]
(b)
Vulture survey fit
Nestor et al. 2005 fit
Vulture survey, $W_r^{\lambda 2796} \geq 0.3$ Å
P(K-S) = 0.112 ± 0.049
Cumulative Distribution
$W_r^{\lambda 2796}$ [Å]

Figure 1. (a) The $W_r^{\lambda 2796} \geq 0.3$ Å equivalent width frequency distribution for The Vulture Survey in black compared to the exponential fit of Nestor et al. (2005), shown as the orange dashed line, and an exponential fit to The Vulture Survey data in purple. The exponential fits are of the form shown in Equation 1. (b) The cumulative distribution of The Vulture Survey data and two comparative exponential fits. The P(K-S) value shown compares our survey's data to the fit from Nestor et al. (2005).

The KODIAQ data sample is reduced and fully continuum fit, delivered as normalized spectra according to the prescriptions of O'Meara et al. (2015). To summarize, observing runs are grouped together and uniformly reduced using HIRedux[3] as part of the XIDL[4] suite of astronomical routines in IDL. Continuum fits are applied one order at a time using Legendre polynomials by a single member of the KODIAQ team, John O'Meara, to minimize bias and variation.

The UVES SQUAD sample also comes reduced and continuum fit according to the prescriptions of King et al. (2012); Bagdonaite et al. (2014); Murphy et al. (2016); Murphy (in prep). Reduction was carried out using the ESO Common Pipeline Language data-reduction software.[5] The continuum is fit automatically with a low order polynomial in small sections using UVES_popler, an ESO/VLT UVES post-pipeline echelle reduction program written by Michael T. Murphy (Murphy 2016). This fit can incorrectly estimate the continuum around narrow emission regions and broad absorption features. Using UVES_popler, we add a higher order continuum fit to such regions of each spectrum, always preserving the continuity of the continuum with non-absorbing regions.

The next step involves detecting all Mg II absorption features. We first limit the search range to regions of the spectrum redward of the Lyα emission, as Lyα forest contamination would render automatic detection of weaker metal lines nearly impossible. We also do not search 5000 km s^{-1} blueward of the quasar emission redshift in order to avoid absorbers associated with the quasar itself. Finally, we exclude regions of strong telluric absorption bands, specifically from 6277 – 6318 Å, 6868 – 6932 Å, 7594 – 7700 Å, and 9300 – 9630 Å, because we found that the molecular line separations and ratios can lead to numerous false positives when searching for Mg II doublets.

To find all intervening Mg II $\lambda\lambda 2796, 2803$ absorbers, we employ a techinque outlined in Zhu & Ménard (2013), in which we perform a matched filter search for absorption candidates detected above a certain S/N threshold. The filter is a top hat function centered at the wavelength of the desired redshifted absorption line. Its width is selected to match the resolution of the spectrum, which is a function of the slit width used during the exposure. A large variety of slit-widths were used to achieve different resolutions for varying science drivers, but, characteristically for a 1.0 arcsec slit, $R \sim 40,000$ for VLT/UVES and $R \sim 45,000$ for Keck/HIRES. We convolve the filter with the normalized spectrum to generate a normalized power spectrum in redshift space, with absorption features having positive power.

The error spectrum in both instruments is complex, irregular, and has frequent single-pixel spikes which makes uniform normalization impossible. Therefore, we cannot convolve the filter with the error spectrum to derive normalized noise estimates, as is often done in matched filter analysis. Instead, we examine the noise in the derived power spectrum. To derive the noise, we first sigma-clip chunks of the power spectrum to remove absorption features, leaving only the continuum power spectrum. Next, we calculate the standard deviation of this continuum. Finally, we use the standard deviation as the noise to calculate the S/N of the absorption features in the power spectrum as the ratio of the normalized power (S) to the normalized noise (N). A flagged absorption feature has $S/N > 5$. A confirmed doublet detetection for Mg II $\lambda\lambda 2796, 2803$ requires detection of $S/N^{\lambda 2796} > 5$ and $S/N^{\lambda 2803} > 3$. In addition, our automated routines remove detections with non-physical doublet ratios in unsaturated regions; specifically, we exclude cases where $W_r^{\lambda 2803} > W_r^{\lambda 2796}$, or $W_r^{\lambda 2803} < \left(0.3 \times W_r^{\lambda 2796}\right)$. The latter constraint is conservative for unsaturated Mg II absorbers, as $W_r^{\lambda 2803}$ is rarely observed less than $0.5 \times W_r^{\lambda 2796}$. We relax this constraint in saturated features. This system could potentially exclude detections where either the Mg II2796 or Mg II2803 line is blended with another transition but does not saturate; however, confirmation of these cases requires extra verification from separate absorbing features, such as Fe II, which are weaker and not always covered in the spectrum.

All absorption features are visually verified upon completion of the detection algorithm. Multiple feature detections

[3] http://www.ucolick.org/ xavier/HIRedux/
[4] http://www.ucolick.org/ xavier/IDL/index.html
[5] http://www.eso.org/observing/dfo/quality/UVES/pipeline/pipe_reduc.html

within ± 500 km s^{-1} of each other are grouped together to generate absorption systems, designated as a single absorber, to be analyzed. Once absorption systems are identified, we calculate the optical depth-weighted median absorption redshift to define the center of the entire absorption system. The formal derivation of this redshift is described in the appendix of Churchill & Vogt (2001).

We also derive an equivalent width detection limit across the spectrum. To do so, we insert modelled Gaussian absorption features across the spectrum and assume a full-width at half maximum (FWHM) defined by the resolution of the instrument to represent unresolved lines. We then solve for the height of the Gaussian, defined as the value at the curve's peak, required to detect the unresolved line with our matched filtering technique at a $S/N = 5$. Finally, we integrate to find the equivalent width, and take that value as the minimum detectable equivalent width at a given wavelength. The detection algorithm is therefore self-monitoring. This full equivalent width detection limit spectrum also allows us to accurately characterize the completeness of our sample, along with the full redshift path length searched.

2.3. *Measuring Absorption Properties*

For each absorption system, we automatically define the wavelength bounds of an absorbing region by finding where the flux recovers to within 1σ of the continuum, with σ defined by the error spectrum, for three pixels on either side of the absorption trough. Within these regions we calculate rest-frame equivalent widths (W_r), velocity widths (Δv), optical depth-weighted kinematic spreads (ω_v), apparent optical depth (AOD) column densities ($\log(N)$), and absorption asymmetries. The functional forms of these parameters are detailed in the appendix of Churchill & Vogt (2001), equations A3 – A7.

3. RESULTS

3.1. *Sample Characterization*

Figure 2 shows the relationships between the measured absorption parameters, characterizing the distribution of absorption properties for our survey. With redshift, there are no obvious trends other than the highest equivalent width absorbers, with $W_r^{2796} > 4$ Å, existing mainly at $z > 1.5$. The data gaps at $z = 1.7$ and $z = 2.4$ represent the larger omitted search regions which overlap with the stronger telluric absorption bands. With column density, we see the normal trends of higher column density systems exhibiting higher equivalent widths and velocity spreads, with the distributions asymptoting near $\log N \simeq 15$ cm^{-2} due to saturation effects and the nature of measuring column densities with the AOD method. Measured column densitites of saturated lines are lower limits. With respect to kinematic spread, we observe the saturation line in the ω_v vs. W_r^{2796} relationship, showing the maximum ω_v for a flat-bottomed absorption profile of a given equivalent width.

3.2. *Sample Completeness and Survey Path Coverage*

To evaluate the completeness and calculate the redshift path coverage of our survey, we use the derived 5σ equivalent width detection limit described at the end of Section 2.2 to determine the number of spectra in which we could detect an absorber of a given equivalent width and redshift. Figure 3 shows the function $g(W_r^{\lambda 2796}, z)$, defined as

$$g(W_j, z_k) = \sum_n H(z_k - z_n^{\min}) H(z_n^{\max} - z_k) H[W_j - 5\sigma_k/(1+z_k)], \quad (2)$$

where H is the Heaviside step function, $z_n^{\min}$ and $z_n^{\max}$ are the minimum and maximum redshifts observed for the nth quasar spectrum, and where the sum extends over all quasar spectra in the sample. This heat map details the number of spectra in which a Mg II $\lambda\lambda 2796, 2803$ doublet could be detected as a function of the equivalent width detection limit and redshift. The vertical stripes with no redshift path coverage represent the omitted telluric absorption regions for our survey. The integral along a given W_r^{2796} slice gives the total redshift path length available for the sample (ΔZ).

3.3. *dN/dz and dN/dX*

The largest sample of quasar spectra originates from the Sloan Digital Sky Survey (SDSS), with more than 10^5 spectra at present, which employs a spectrograph with an instrumental resolution around 69 km s^{-1}, limiting SDSS absorption surveys to strong absorbers, with $W_r^{\lambda 2796} \geq 0.3$ Å (Nestor et al. 2005; Zhu & Ménard 2013). Conversely, previous studies of weak absorbers used small samples of quasar spectra, never exceeding 100 quasar spectra (Steidel & Sargent 1992; Narayanan et al. 2007; Kacprzak et al. 2011). In this paper, we aim to characterize the evolution of the incidence rate, number of absorbers per redshift path length, comoving line density, and cosmic mass density of all Mg II absorbers from redshifts $0.18 < z < 2.57$.

The number of Mg II absorbers per redshift path length and its associated variance are defined as

$$\frac{dN}{dz} = \sum_i \frac{1}{\Delta Z_i(W_r)}, \quad \sigma^2_{\frac{dN}{dz}} = \sum_i \left[\frac{1}{\Delta Z_i(W_r)}\right]^2, \quad (3)$$

where we count the number of Mg II absorbers, dividing by the total searched redshift path length (ΔZ), defined as

$$\Delta Z_i(W_r) = \int_{z_1}^{z_2} g_i(W_r, z)\, dz, \quad (4)$$

where $g_i(W_r, z)$ is the equivalent width sensitivity function at a given equivalent width detection limit shown in Equation 2. The function $g(W_r, z)$, first formulated in Lanzetta et al. (1987), details the number of spectra in which an absorption feature with a given equivalent width may be detected at the 5σ level in a given redshift interval.

The comoving Mg II line density and its associated variance are defined as

$$\frac{dN}{dX} = \sum_i \frac{1}{\Delta X_i(W_r)}, \quad \sigma^2_{\frac{dN}{dX}} = \sum_i \left[\frac{1}{\Delta X_i(W_r)}\right]^2, \quad (5)$$

where we count the number of Mg II absorbers, dividing by the total searched absorption path (ΔX), defined as

$$\Delta X_i(W_r) = \int_{z_1}^{z_2} g_i(W_r, z) \frac{(1+z)^2}{\sqrt{\Omega_M (1+z)^3 + \Omega_\Lambda}}\, dz, \quad (6)$$

where Ω_M is the cosmic matter density, and Ω_Λ is the cosmic density attributed to dark energy. Counting with respect to ΔX accounts for both cosmological expansion along the

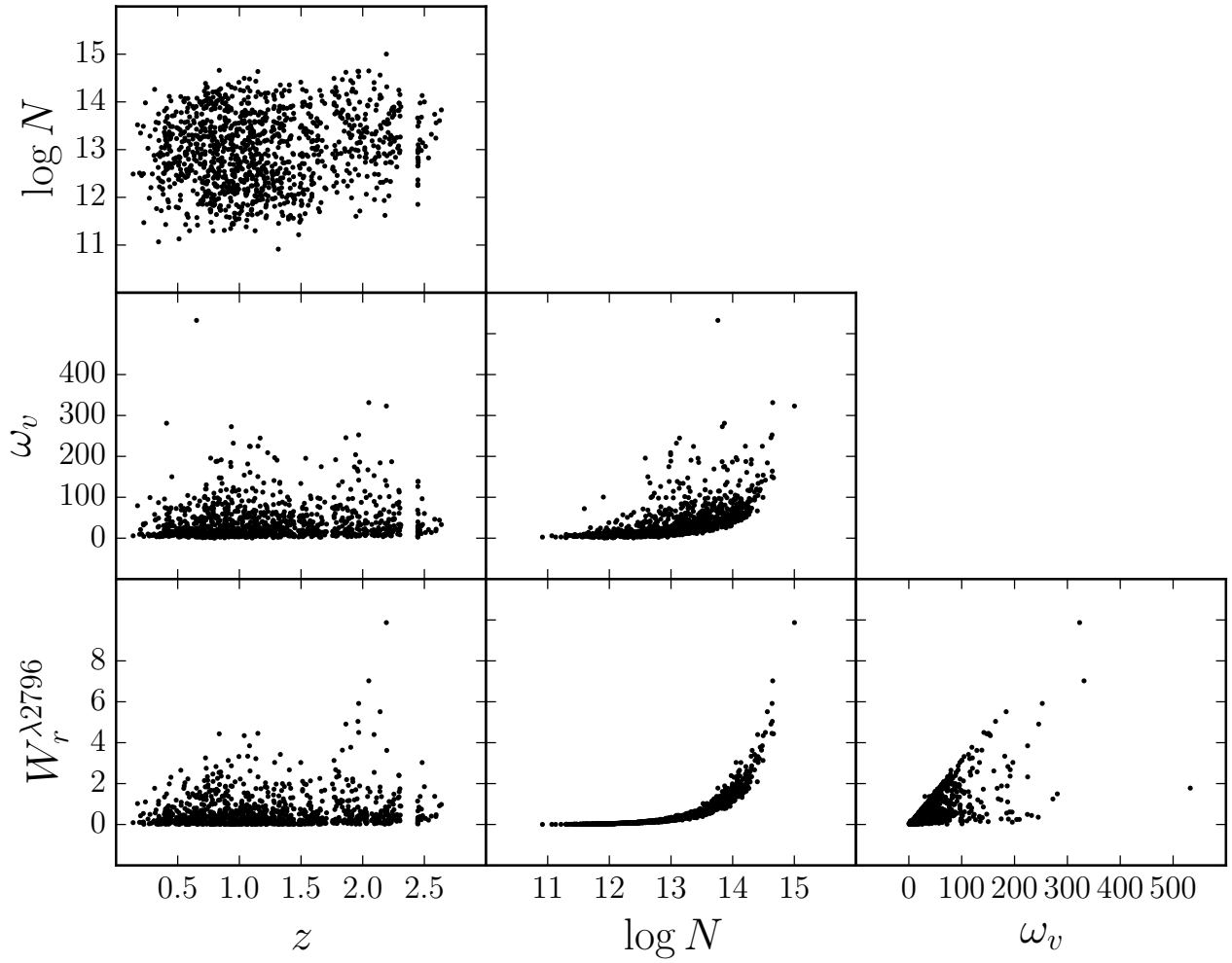

Figure 2. Correlations between measured absorption properties for The Vulture Survey. $\log N$ is the Mg II AOD column density, ω_v is the kinematic spread, W_r^{2796} is the rest frame Mg II2796 equivalent width, and z is the absorption redshift.

line of sight and the transverse separation of objects with unchanging number density and cross section, allowing for more consistent comparisons across redshift.

In Figure 4, we plot dN/dz and dN/dX, respectively, as a function of redshift for different minimum equivalent width thresholds, such that detected Mg II absorbers have equivalent widths greater than $W_{r,\rm min}^{\lambda 2796}$. Error bars in each bin represent 1σ uncertainties calculated according to Equations 3 and 5. Dotted lines are fit according to the analytical form which allows for redshift evolution in dN/dX, defined as,

$$f(z) \equiv \frac{c}{H_o} n(z)\,\sigma(z) = \frac{c}{H_o} n_0\,\sigma_0\,(1+z)^{\epsilon}, \qquad (7)$$

where c is the speed of light, H_o is the Hubble Constant, n_0 is the comoving number density of Mg II absorbers at $z = 0$, σ_0 is the absorbing cross-section at $z = 0$, and ϵ is the evolution parameter, defined as the power dependence of dN/dX on redshift. The product $n_0\,\sigma_0$ represents a comoving opacity of Mg II-selected absorption line systems by virtue of the units, which are an inverse path length, and the analogous absorption coefficient to describe the opacity of material in stellar atmospheres. The full product of $\frac{c}{H_o} n_0\,\sigma_0$ then represents the comoving Hubble optical depth for Mg II absorbers. We find that the best-fit value of ϵ is negative when analyzing the full sample of Mg II absorbers, including all detections with measured equivalent widths above $W_r^{\lambda 2796} > 0.01$ Å. The evolution parameter, ϵ, then increases with subsequently larger minimum equivalent width thresholds, becoming positive for absorbers with $W_{r,\rm min}^{\lambda 2796} > 1.0$ Å. This trend is driven primarily by an enhancement in dN/dX for the strongest Mg II absorbers around $z \sim 2$, relative to lower redshifts. Conversely, at low redshift we observe more weak Mg II absorbers per absorption path length. We show in Table 1 the values of the fit parameters for varying $W_{r,\rm min}^{\lambda 2796}$, along with their 1σ uncertainties.

In Figure 5, we show the values of $\frac{c}{H_o} n_0\,\sigma_0$ and ϵ as a function of $W_{r,\rm min}^{\lambda 2796}$. The shaded red areas represent the 1σ standard deviations derived from the fits to the dN/dX distribution. We show first that the comoving Hubble optical depth of Mg II absorbers decreases as a function of $W_r^{\lambda 2796}$. This implies that, per unit absorption path length, there are fewer high equiva-

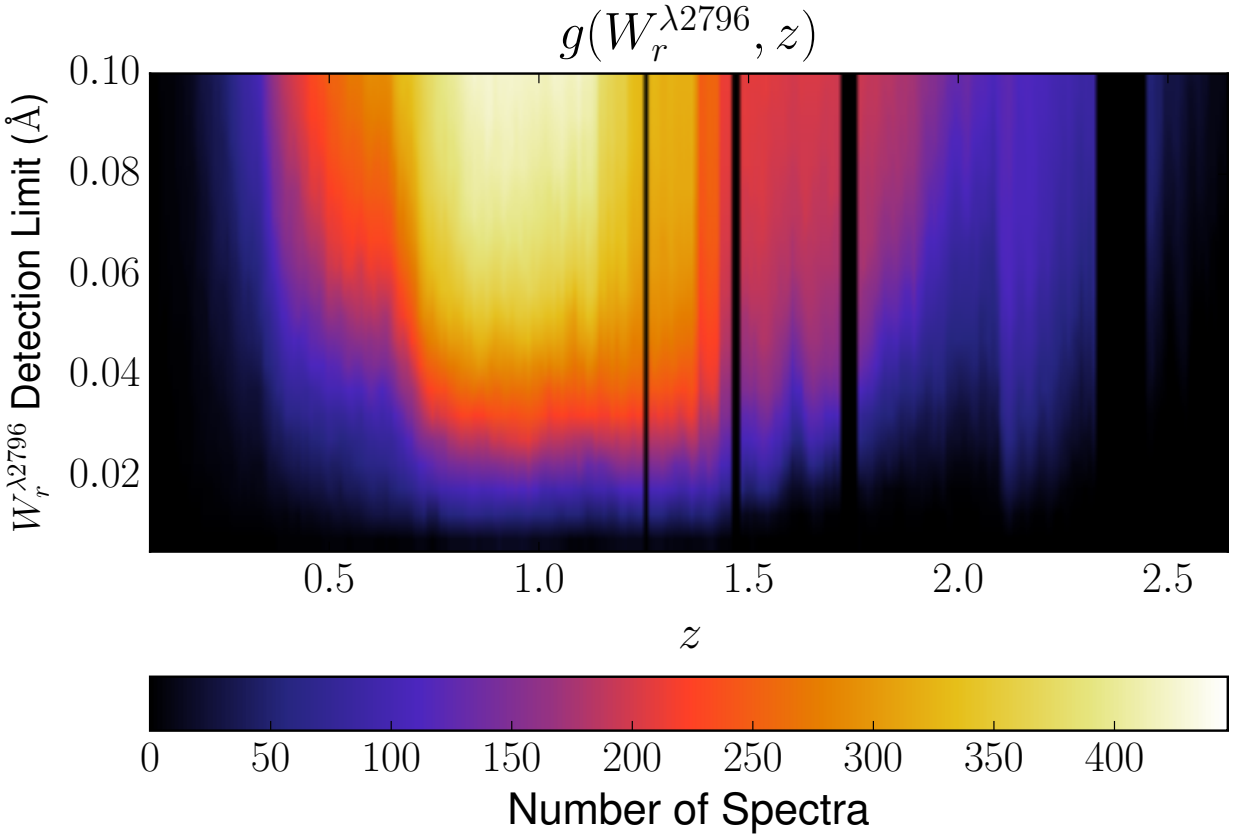

Figure 3. The function $g(W_r^{\lambda 2796}, z)$ shown as a heat map with the colors representing the value of $g(W_r^{2796}, z)$. This is the number of spectra in which an absorption line of a given equivalent width and a given redshift may be detected according to the detection limit of the spectrum. The vertical black bars representing no redshift path length coverage show the omitted wavelength regions of the survey based upon contaminating telluric absorption features.

Table 1
Parameterization of dN/dX

$W_{r,\min}^{2796}$ [Å]	$\frac{c}{H_o} n_0 \sigma_0$	ϵ
0.01	2.583 ± 0.827	-1.04 ± 0.38
0.30	0.446 ± 0.076	-0.14 ± 0.21
1.00	0.116 ± 0.043	0.31 ± 0.44
0.01	0.019 ± 0.014	0.94 ± 0.85

lent width Mg II absorbers, and/or that they exist in smaller absorbing structures. We also show that the slope of the redshift dependence, ϵ, increases as a function of increasing $W_{r,\min}^{\lambda 2796}$. This evolution parameter, ϵ, changes from negative to positive toward higher equivalent width Mg II absorbers, implying that strong Mg II absorbers evolve away, decreasing in relative number per absorption path length, from $z = 2$ to present. Conversely, weak Mg II absorbers build up over time, increasing in relative number per absorption path length from $z = 2$ to present. We observe no evolution with redshift in absorbers with equivalent widths between $0.3 < W_r^{\lambda 2796} < 1$ Å.

We provide a parameterized fit to $\frac{c}{H_o} n_0 \sigma_0$ and ϵ as a function of $W_{r,\min}^{\lambda 2796}$. In Figure 5(a), we adopt a power-law with a generalized exponential decay to model the $\frac{c}{H_o} n_0 \sigma_0$ distribution, defined as,

$$\frac{c}{H_o} n_0 \sigma_0(\psi) = \Psi^*(\psi)^\alpha e^{-\psi^\beta}, \quad (8)$$

where $\psi = W_{r,\min}^{\lambda 2796} / W_{r,\min}^*$ to simplify the equation. The best fit parameters are $\Psi^* = 0.24 \pm 0.01$, $W_{r,\min}^* = 1.19 \pm 0.02$, $\alpha = -0.49 \pm 0.01$, and $\beta = 1.50 \pm 0.05$. This parameterization resembles a Schechter function, but we required an exponential drop-off at the high end faster than e^{-x}, which manifests itself in the form of β. Next, in Figure 5(b), we fit a broken power-law to the ϵ distribution, defined as,

$$\epsilon(W_{r,\min}^{\lambda 2796}) = \begin{cases} a_1 (W_{r,\min}^{\lambda 2796})^{\gamma_1} + b_1 & \text{if } W_{r,\min}^{\lambda 2796} < 1.1 \text{ Å} \\ a_2 (W_{r,\min}^{\lambda 2796})^{\gamma_2} + b_2 & \text{if } W_{r,\min}^{\lambda 2796} \geq 1.1 \text{ Å}, \end{cases} \quad (9)$$

where the fit parameters for minimum equivalent width

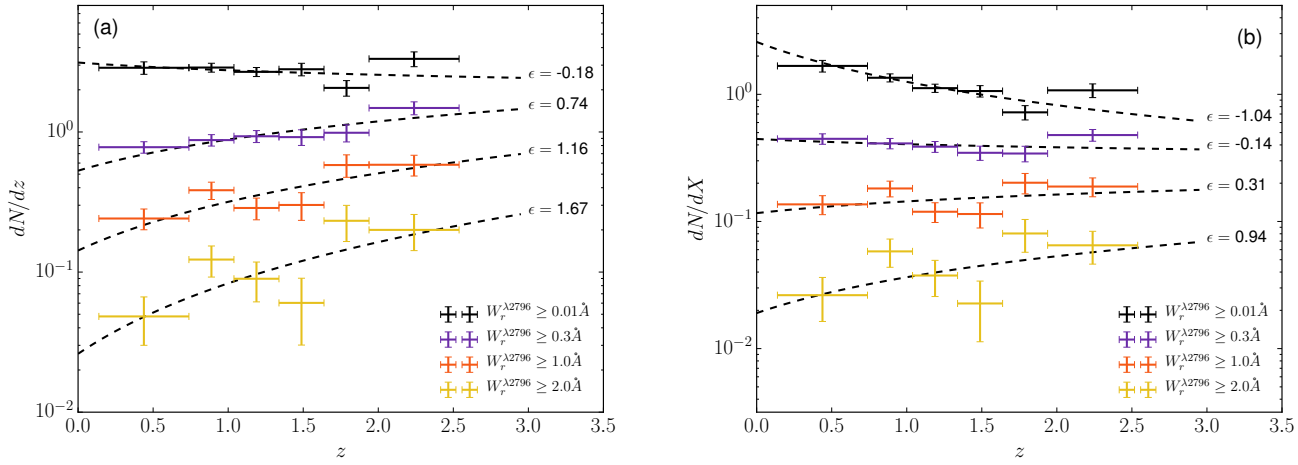

Figure 4. (a) dN/dz and (b) dN/dX as a function of redshift for different minimum equivalent width thresholds, $W_{r,\mathrm{min}}^{\lambda2796}$. Colors represent different $W_{r,\mathrm{min}}^{\lambda2796}$. The black dotted lines are fits to the distribution of the functional form $f(z) = \frac{c}{H_o} n_0 \sigma_0 (1+z)^{\epsilon}$, with the best fit ϵ value labelled. We see increasing values of ϵ with increasing equivalent width, driven by an enhancement of stronger Mg II absorbers around redshift 2 compared to lower redshifts. Vertical error bars represent 1σ uncertainties in each bin.

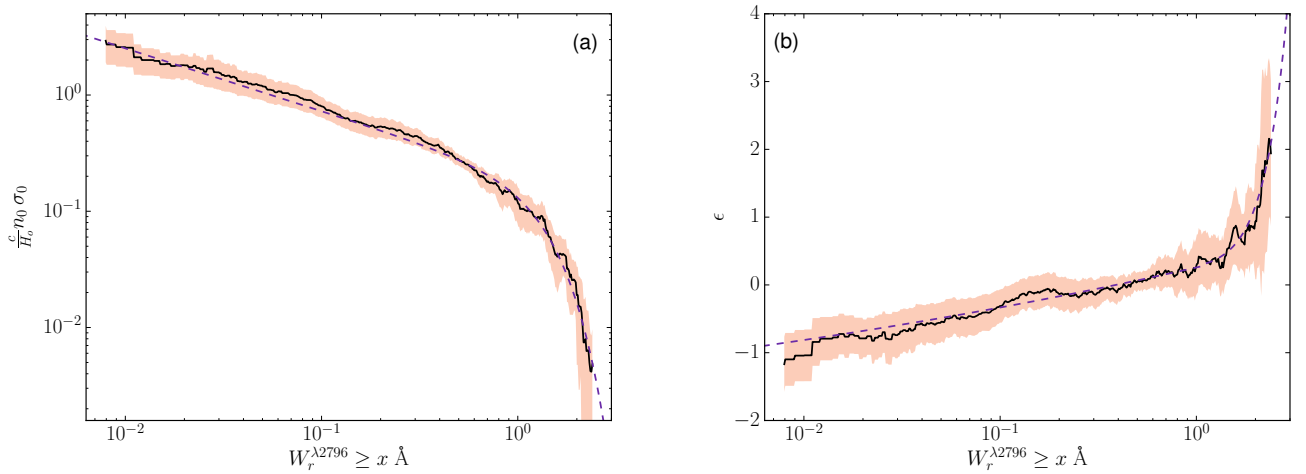

Figure 5. (a) The comoving number density of absorbers multiplied by the absorbing cross-section, derived by fitting Equation 7 to dN/dX, as a function of $W_{r,\mathrm{min}}^{\lambda2796}$ with shaded 1σ uncertainties. As we examine samples with increasing minimum Mg II equivalent width thresholds, either the space density of absorbing cloud structures decreases, the absorbing cross-section decreases, or both parameters decrease. (b) The redshift evolution parameter, ϵ, as a function of $W_{r,\mathrm{min}}^{\lambda2796}$. Weak Mg II absorbers are more abundant at low redshift, leading to a negative coefficient ϵ. Absorbers with equivalent widths near 0.3 Å do not evolve, with $\epsilon \simeq 0$. Strong Mg II absorbers evolve away at low redshift, showing a large positive ϵ increasing towards $z \sim 2$.

thresholds below 1.1 Å are $a_1 = 3.13 \pm 1.49$, $\gamma_1 = 0.09 \pm 0.05$, and $b_1 = 2.87 \pm 1.49$. The fit parameters for the power-law with $W_{r,\mathrm{min}}^{\lambda2796} \geq 1.1$ Å are $a_2 = 0.07 \pm 0.01$, $\gamma_2 = 3.73 \pm 0.25$, and $b_2 = -0.21 \pm 0.03$. Combining the fits to $\frac{c}{H_o} n_0 \sigma_0$ and ϵ, we now have an analytic parameterization of dN/dX as a function of $W_{r,\mathrm{min}}^{\lambda2796}$, and z, of the form,

$$\frac{dN}{dX}(W_{r,\mathrm{min}}^{\lambda2796}, z) = \Psi^* \psi^{\alpha} e^{-\psi^{\beta}} (1+z)^{\epsilon(W_{r,\mathrm{min}}^{\lambda2796})}. \quad (10)$$

This function can be used in future semi-analytic models to parameterize the physical properties of Mg II absorbers in galaxy halos (e.g. Shattow et al. (2015)).

3.4. *Equivalent Width Frequency Distribution*

To calculate the equivalent width frequency distribution $f(W)$, the number of absorbers of a given equivalent width per unit path density, we calculate dN/dz or dN/dX for each equivalent width bin and divide by the bin width. We split the sample into four redshift regimes, ensuring that the number of absorbers in each redshift subsample remains constant. The result is a characteristic number of Mg II absorbers per redshift or absorption path length per equivalent width.

In Figure 6, we plot the equivalent width frequency distribution with respect to either dN/dz or dN/dX. We fit each distribution with a Schechter function of the form,

$$\Phi(W_r) = \Phi^* \left(\frac{W_r}{W_r^*}\right)^{\alpha} e^{-W_r/W_r^*}, \quad (11)$$

where Φ^* is the normalization, α is the low equivalent width

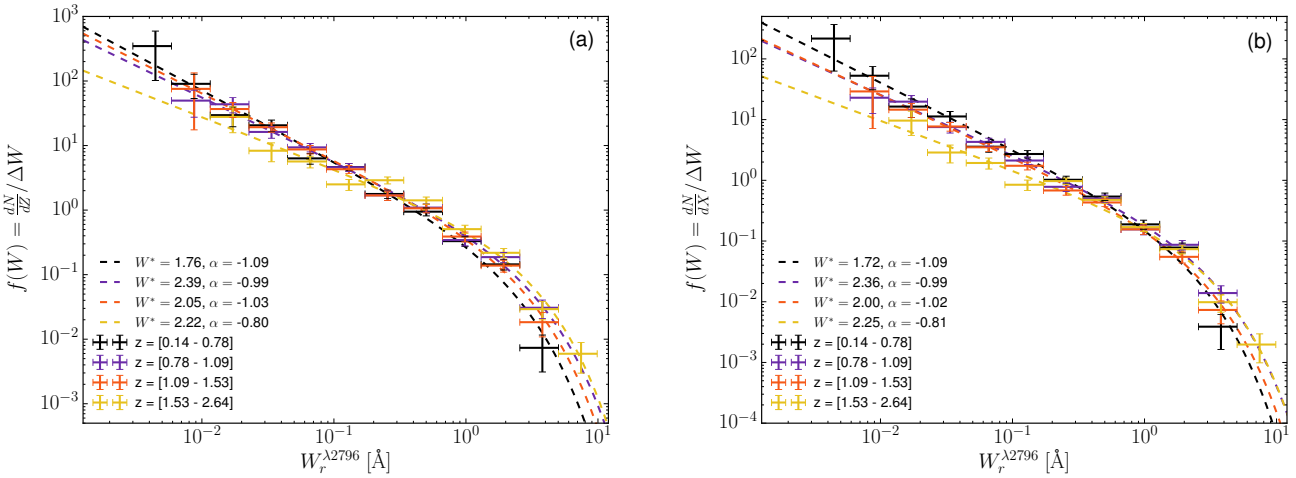
(a)
$f(W) = \frac{dN}{dz}/\Delta W$
$W^* = 1.76, \alpha = -1.09$
$W^* = 2.39, \alpha = -0.99$
$W^* = 2.05, \alpha = -1.03$
$W^* = 2.22, \alpha = -0.80$
z = [0.14 - 0.78]
z = [0.78 - 1.09]
z = [1.09 - 1.53]
z = [1.53 - 2.64]
$W_r^{\lambda 2796}$ [Å]
(b)
$f(W) = \frac{dN}{dX}/\Delta W$
$W^* = 1.72, \alpha = -1.09$
$W^* = 2.36, \alpha = -0.99$
$W^* = 2.00, \alpha = -1.02$
$W^* = 2.25, \alpha = -0.81$
z = [0.14 - 0.78]
z = [0.78 - 1.09]
z = [1.09 - 1.53]
z = [1.53 - 2.64]
$W_r^{\lambda 2796}$ [Å]

Figure 6. (a) The equivalent width distribution of Mg II absorbers, defined as the redshift path density (dN/dz) in each equivalent width bin divided by the bin width. (b) The equivalent width distribution, defined as the comoving line density (dN/dX) in each equivalent width bin divided by the bin width. Error bars represent 1σ uncertainties in each bin. We fit each distribution with a Schechter function, capturing the self-similar power-law behavior of weak Mg II absorbers and the exponential power-law cutoff when observing the strongest Mg II systems.

Table 2
Schechter Fit to $f(W) = \frac{dN}{dX}/\Delta W$

Redshift Range	Φ^*	W^* [Å]	α
0.14 – 0.78	0.15 ± 0.10	1.72 ± 0.68	-1.09 ± 0.09
0.78 – 1.09	0.12 ± 0.06	2.36 ± 0.81	-0.99 ± 0.06
1.09 – 1.53	0.11 ± 0.03	2.00 ± 0.35	-1.02 ± 0.04
1.53 – 2.64	0.12 ± 0.08	2.25 ± 0.87	-0.81 ± 0.12

Table 3
Schechter Fit to $f(N) = \frac{dN}{dX}/\Delta N$

Redshift Range	Φ^* [$\times 10^{-16}$]	N^* [$\times 10^{14}$ cm^{-2}]	α
0.14 – 0.78	8.79 ± 8.19	1.71 ± 0.97	-1.14 ± 0.08
0.78 – 1.09	6.41 ± 2.43	2.29 ± 0.56	-1.10 ± 0.03
1.09 – 1.53	4.15 ± 2.40	2.65 ± 1.00	-1.12 ± 0.04
1.53 – 2.64	7.98 ± 6.51	2.35 ± 1.32	-0.91 ± 0.08

power-law slope, and W_r^* is the turnover point in the distribution where the low equivalent width power-law slope transitions into an exponential cutoff. Table 2 shows the values of Φ^*, W_r^*, and α, along with their associated 1σ uncertainties derived from the fitting routine. This functional fit is motivated by papers such as Kacprzak & Churchill (2011), where the authors seek to combine previous surveys of strong Mg II absorbers, in which exponential fits were preferred, and surveys of weak Mg II absorbers, where power-laws best fit the equivalent width distribution. The power-law nature of the distribution of weak absorbers in our survey is apparent, and the exponential cutoff is motivated by physical limits to the size, density, and velocity widths of Mg II absorbing clouds. Examining the distribution as a function of redshift, we find the low equivalent width slope becomes more shallow at $z \sim 2$ compared with the present epoch, with $\alpha = -1.09$ in our subsample with $0.14 \leq z < 0.78$ and $\alpha = -0.81$ in our subsample with $1.53 < z \leq 2.64$. We observe fewer weak Mg II absorbers and more strong Mg II absorbers per redshift/comoving absorption path length at $z \sim 2$ than we do at $z \sim 0.5$.

3.5. *Column Density Distribution*

To calculate the column density distribution, the number of absorbers of a given column density per unit path density, we calculate dN/dz or dN/dX for each column density bin and divide by the bin width. The result is a characteristic number density of Mg II absorbers per redshift or absorption path length as a function of their column densities. It should be noted that at high column densities near $\log(N(\mathrm{Mg\,II}))$ = 15 cm^{-2}, the measured column densities are lower limits as the AOD method cannot constrain the true column when the absorption line becomes saturated.

In Figure 7, we plot the column density frequency distribution using either dN/dz or dN/dX. Again, we fit this distribution with a Schechter function of the same form as Equation 11, except with equivalent width replaced with column density. Table 3 shows the values of Φ^*, N^*, and α, along with their associated 1σ uncertainties. We find again that the low column density slope is shallower near $z \sim 2$ than at $z \sim 0.5$. Due to saturation effects, the highest column density measurements are lower limits; therefore, the final high column density bin in $f(N)$ should be regarded as an upper limit. These limits are taken into account in the functional fitting procedures.

3.6. $\Omega_{\mathrm{Mg\,II}}$

We now aim to calculate the matter density of Mg II absorbers across cosmic time. To do so, we employ the following customary equation relating the mass density of an ion as a fraction of the critical density today to the first moment of the column density distribution,

$$\Omega_{\mathrm{Mg\,II}} = \frac{H_0\, m_{\mathrm{Mg\,II}}}{c\, \rho_{c,0}} \int_{N_{min}}^{N_{max}} f(N_{\mathrm{Mg\,II}}) N_{\mathrm{Mg\,II}}\, dN_{\mathrm{Mg\,II}}, \qquad (12)$$

where H_0 is the Hubble constant today, $m_{\mathrm{Mg}} = 4.035 \times 10^{-23}$ g, c is the speed of light, $\rho_{c,0}$ is the critical density at present, $f(N_{\mathrm{Mg\,II}})$ is the column density distribution of Mg II absorbers,

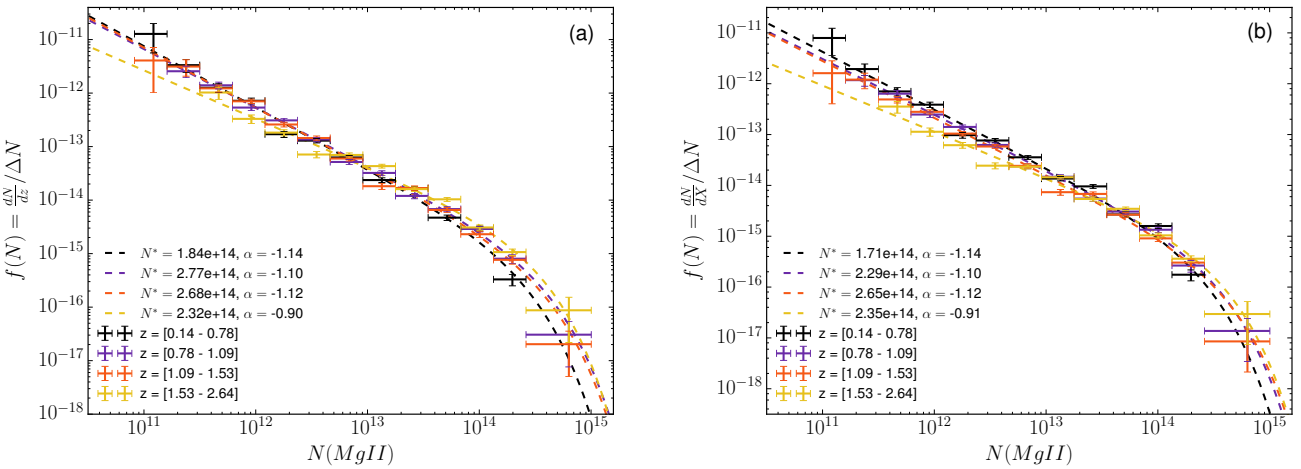
(a)
(b)
$f(N) = \frac{dN}{dz}/\Delta N$
$f(N) = \frac{dN}{dX}/\Delta N$
$N(MgII)$
$N^* = 1.84e+14, \alpha = -1.14$
$N^* = 2.77e+14, \alpha = -1.10$
$N^* = 2.68e+14, \alpha = -1.12$
$N^* = 2.32e+14, \alpha = -0.90$
$N^* = 1.71e+14, \alpha = -1.14$
$N^* = 2.29e+14, \alpha = -1.10$
$N^* = 2.65e+14, \alpha = -1.12$
$N^* = 2.35e+14, \alpha = -0.91$
z = [0.14 - 0.78]
z = [0.78 - 1.09]
z = [1.09 - 1.53]
z = [1.53 - 2.64]

Figure 7. (a) The column density distribution of Mg II absorbers, defined as the redshift path density (dN/dz) in each column density bin dividided by the bin width. (b) The comoving line density (dN/dX) in each column density bin divided by the bin width. We fit this distribution with a Schechter function to accurately parameterize the low column density power-law slope and the exponential cutoff and high column densities.

and $N_{\rm Mg II}$ is the column density. Using our derived fit to the column density distribution, we are able to numerically integrate the first moment from $0 < \log N({\rm Mg\,II}) < 20$ cm^{-2}. The results are shown below in Figure 8. 1σ uncertainties are derived with a bootstrap Monte-Carlo method. We select random column densities, with replacement, from the sample of measured column densities for all of our Mg II absorbers until we reach the sample size. We then recalculate the column density distribution, find the best parameterized Schechter fit, and then integrate and compute Equation 12. We perfom this task 1499 times to develop a statistical ensemble of values for Ω, with this number of samples representing the underlying scatter in the $\Omega_{\rm Mg II}$ distribution at the 99% confidence level according to Davidson & MacKinnon (2000). We take the standard deviation about the mean of this ensemble of simulated measurements as the 1σ uncertainty in Ω_{MgII}. We find that the cosmic mass density of Mg II increases from $\Omega_{\rm Mg II} \simeq 0.8 \times 10^{-8}$ at $z \sim 0.5$ to $\Omega_{\rm Mg II} \simeq 1.3 \times 10^{-8}$ at $z \sim 2$.

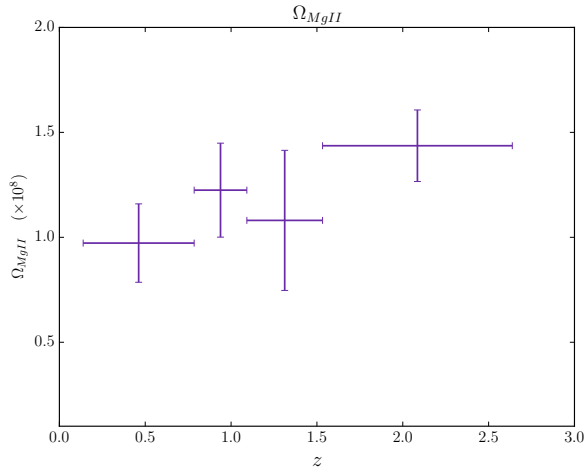

Figure 8. $\Omega_{\rm Mg II}$ as a function of redshift. The cosmic mass density of Mg II stays roughly flat near a value of 1×10^{-8}, with a 0.5 dex increase from $z \sim 0.5$ to $z \sim 2$.

4. DISCUSSION

We have shown a cosmic inventory of Mg II absorbing gas from $0.1 < z < 2.6$, measuring dN/dz, dN/dX, the equivalent width distribution, and the column density distribution down to detection limits as low as $W_r^{\lambda 2796} = 0.01$ Å. We aim now to relate the properties of Mg II absorbers and their evolution across cosmic time to other known evolutionary processes with the hope of gaining insight into the mechanisms which give rise to Mg II absorbing gas.

4.1. *Evolution of* Mg II *Distributions*

Narayanan et al. (2007) measured the evolution of weak Mg II absorbers from $0.4 < z < 2.4$ in VLT/UVES spectra. They compared to Churchill et al. (1999), who fitted the equivalent width frequency distribution with a power-law, and to Nestor et al. (2005), who fitted an exponential to $f(W_r)$. In the case of weak absorbers at $z < 1.4$, Narayanan et al. (2007) found that a power-law with a slope of $\alpha = -1.04$ is a satisfactory fit, confirming the results of Churchill et al. (1999). When they split their sample into low redshift, with detections between $0.4 < z < 1.4$, and high redshift, with detections between $1.4 < z < 2.4$, they found that the low redshfit sample remained consistent with a power-law but the high redshift sample was best fit by an exponential function. Our data show that a faint end power-law slope of $\alpha = -0.81$ is appropriate for the higher redshift subsample, and we note that this is also consistent with the data of Narayanan et al. (2007).

Narayanan et al. (2007) also analyzed the evolution of dN/dz with redshift for weak Mg II absorbers. They found that the distribution follows the "no evolution" expectation; that is, the expected number density for a nonevolving population of absorbers in a ΛCDM universe, at redshifts less than $z = 1.5$. At higher redshift, they found that dN/dz for weak absorbers decreases below the no evolution expectation. In Figure 9(a) we make a direct comparison with Narayanan et al. (2007), showing dN/dz for $0.02 \leq W_r^{\lambda 2796} < 0.3$ Å binned in the same manner as their Figure 4. Here, we observe that the apparent peak in dN/dz for weak absorbers occurs near $z = 0.75$, as opposed to $z = 1.2$ in Narayanan et al. (2007). However, the overall shape of dN/dz for this low equivalent width population remains in good agreement, with

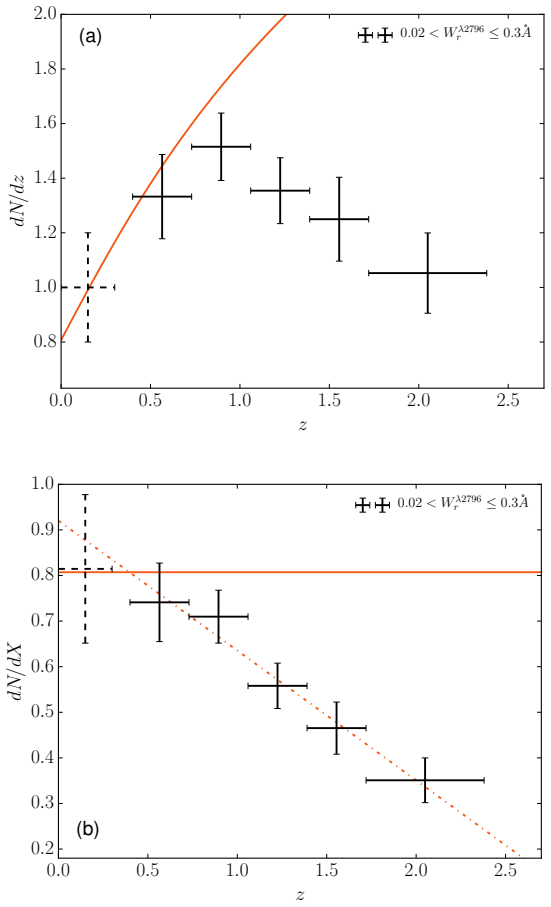

Figure 9. (a) dN/dz as a function of redshift for equivalent widths in the range $0.02 < W_r^{\lambda2796} \leq 0.3$ Å. We also include the survey data point from $0 < z < 0.3$ of Narayanan et al. (2005) as shown by the dashed histogram. (b) dN/dX as a function of redshift for the same population. Error bars represent 1σ uncertainties as calculated in Equations 3 and 5. The red solid lines represent the no-evolution expectation, normalized at $z = 0.9$ and $dN/dz = 1.74$, matching Narayanan et al. (2007). The red dot-dashed line in panel (b) represents a linear fit to the binned data of the form $dN/dX = -0.28^{(\pm0.04)}z + 0.92^{(\pm0.04)}$. By this construction, $dN/dX = 0$ at $z = 3.3$, implying we should detect no weak Mg II absorbers past this redshift. This equivalent width range comprises exclusively "weak" Mg II absorbers.

the number of weak absorbers per redshift path length rising from $z = 0.4$ to $z \sim 1.0$, following the no evolution expectation, and then falling well below that expectation from $z \sim 1.0$ to $z \sim 2.4$. In Figure 9(b), we show dN/dX for weak Mg II absorbers. Here, we clearly see evolution in the distribution of low equivalent width absorbers, showing that the comoving line density of weak Mg II absorbers steadily decreases as a function of redshift from $z = 0.4$ to $z = 2.4$. The "no evolution" assumption would be a perfectly flat distribution, as shown by the solid red line. We also fit a linear approximation to the binned data of Figure 9(b) of the form $dN/dX = -0.28\,(\pm0.04)z + 0.92\,(\pm0.04)$, including the lowest redshift data point taken from Narayanan et al. (2005). This function shows dN/dX going to zero at $z = 3.3$, implying that no Mg II absorbers with equivalent widths between $0.02 < W_r^{\lambda2796} \leq 0.3$ Å should be detected above this redshift. In other words, weak Mg II absorbers are predicted not to exist at redshifts above $z = 3.3$ by this trend. This evolution follows similar trends to the evolution in cosmic metallicity and ionizing background intensity, such that we detect more weak Mg II absorbers at low redshift, where the metallicity of the CGM is higher and the ionizing background is less likely to destroy Mg II, as opposed to higher redshifts, where the opposite applies.

Steidel & Sargent (1992), and later Nestor et al. (2005), examined the redshift evolution of dN/dz for strong Mg II absorbers with $W_r^{\lambda2796} > 0.3$ Å. They found that the number of strong Mg II absorbers per redshift path length increases as a function of redshift from $z = 0$ to $z = 2.2$; however, they could not derive the slope of this trend to sufficient accuracy to distinguish between an evolving population or a non-evolving population. We perform a similar analysis on our sample, calculating instead dN/dX, where a flat distribution implies no evolution. When we take absorbers with $W_r^{\lambda2796} > 0.3$ Å, we find that a fit to the function $dN/dX = \frac{c}{H_o} n_0 \sigma_0 (1+z)^\epsilon$ with a slope of $\epsilon = -0.20 \pm 0.22$ is appropriate, implying that the comoving number density and/or cross-section of strong Mg II absorbers does not significantly evolve. However, when considering even stronger absorbers with $W_r^{\lambda2796} > 1$ Å, we do observe evolution in dN/dX, with the evolution parameter, ϵ, becomming positive and increasing, as shown in Figure 5. This evolution does not seem to be influenced by either an increase in the cosmic metallicity at low redshifts, or a decrease in the intensity of the cosmic ionizing background near the present epoch, which should produce more favorable conditions for Mg II absorbing gas. In fact, in order to seemingly oppose these factors, we must infer an increase in the total quantity of Mg II absorbing gas, observed as high equivalent width Mg II systems, outside galaxies near $z = 2$. In Section 4.2, we will explore the physical processes responsible for evolution in the universal distribution of Mg II absorbing gas.

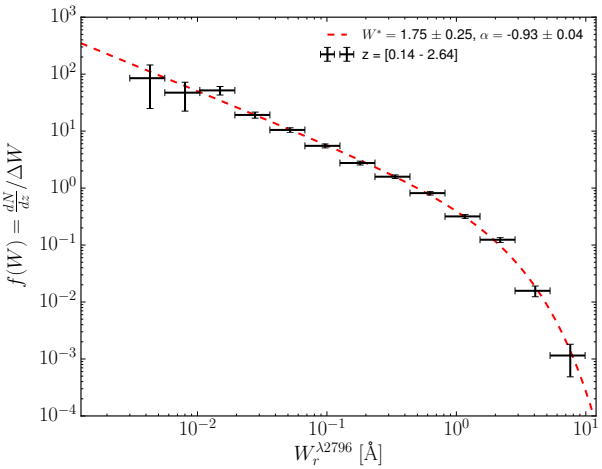

Figure 10. The equivalent width distribution of all detected Mg II absorbers, defined as the redshift path density (dN/dz) in each equivalent width bin divided by the bin width. The cosmic distribution of absorbing Mg II is well fit by a Schechter function, with the parameters detailed in Equation 11.

Kacprzak & Churchill (2011) combined multiple previous studies to characterize the equivalent width distribution function, $f(W_r)$. It is important to note, for comparison, that their sample with $W_r < 0.3$ Å spans redshifts from $0.4 \leq z \leq 1.4$, while their sample with $W_r \geq 0.3$ Å spans $0.4 \leq z \leq 2.3$. They found a Schechter function with a low equivalent width slope of $\alpha = -0.642 \pm 0.062$ and a characteristic equivalent width

for the exponential cutoff of $W^* = 0.97 \pm 0.06$ Å best fit the data, within the reported 1σ uncertainties. In Figure 10, we perform the same analysis with the total sample of our survey, finding $\alpha = -0.91 \pm 0.04$ and $W^* = 1.69 \pm 0.26$ Å. The point of tension between these studies lies in the value of the low equivalent width slope. Kacprzak & Churchill (2011) combine very different surveys in order to sample the full equivalent width distribution, leading to a non-uniform data set. Specifically at the low equivalent end of the distribution, we note that the error in their determination of α is smaller than the scatter in the data. In private communication with the authors, they speculate that differences in the analysis methods of low equivalent width Mg II absorption line surveys lead to unaccounted systematics and an underestimation of the error in their functional fits.

At redshifts beyond $z \sim 2.5$, the works of Matejek & Simcoe (2012), Matejek et al. (2013), and Chen et al. (2016) described the detection statistics of strong Mg II absorbers up to $z = 7$ using the Magellan/FIRE spectrograph. They found that dN/dX for all absorbers with $W_r^{\lambda 2796} > 0.3$ Å does not evolve from $z = 0.25$ to $z = 7$. However, restricting their sample to the absorbers with $W_r^{\lambda 2796} > 1.0$ Å, they found approximately a factor of 2 increase in number density at $z = 2-3$ compared to $z = 0$. At redshifts above $z = 3$, dN/dX declines by an order of magnitude by $z \sim 6$. Converting Mg II equivalent widths into an effective contribution to the global star formation rate using the methods of Ménard et al. (2011) and comparing them to the total galaxy star formation rate density derived from observations of deep fields, they found exceptional agreement in the evolutionary trends of both distributions at all redshifts. The incidence of strong Mg II absorbers at all redshifts is tied to star formation.

4.2. *Potential Causes for Trends*

The most obvious conclusion to be drawn from our analysis of Mg II absorbers in The Vulture Survey is that the physical conditions affecting Mg II absorbers change as a function of redshift. When we compare the sample of Mg II absorbers at $z \sim 0.5$ to the sample of absorbers at $z \sim 2$, we find the following statements are true of the higher redshift sample:

1. There are more strong Mg II absorbers per redshift path length and per absorption path.
2. The faint end slope of the equivalent width and column density distributions is flatter.
3. The "knee" of the Shechter fit to the equivalent width and column density distributions lies at higher values of $W_r^{\lambda 2796}$ and N(Mg II).
4. The cosmic mass density of Mg II is larger.

We can now state that the physical properties driving the global distribution of Mg II absorbers at $z \sim 0.5$ are different than at $z \sim 2$. In addition, these physical properties do not affect all Mg II systems equally. If we examine weak systems alone, we find that these low equivalent width absorbers follow a no-evolution expectation from present day up to $z \sim 1$, at which point they decrease in number per absorption path length rapidly until $z \sim 2.5$. If we examine the strongest systems, those with $W_r^{\lambda 2796} > 1.0$ Å, we find the opposite behavior, where these absorbers are more numerous at $z \sim 2.5$ than at $z \sim 0.5$. Possible explanations relate to the ionization conditions in the halos of galaxies at this time, the metallicity of gas around galaxies, and/or the quantity of metals in the circumgalactic medium, which we will now explore.

Haardt & Madau (2012) represents the most recent estimate of the cosmic ionizing background as a function of redshift, which is the primary ionizing component responsible for the universal ionization state of gas in galactic halos. The authors found that the comoving 1 Ryd emissivity is an order of magnitude higher at $z = 1$ compared to the present epoch, and nearly two orders of magnitude larger at $z = 2$ than at present. As the number of ionizing photons in the IGM increases with increasing redshift, holding constant the density and quantity of metals in galactic halos, we would nominally expect for the ionization parameter of absorbers in the halos of galaxies to increase with redshift. Increasing the ionization parameter alone should decrease the observed quantity of Mg II, as it favors lower ionization parameter conditions. The comoving line density (dN/dX) of Mg II absorbers with equivalent widths below $W_r^{\lambda 2796} < 0.3$ Å declines linearly with increasing redshift, following the expectation that a more intense ionizing background at higher redshift disfavors Mg II absorption. However, when examining absorbers with $W_r^{\lambda 2796} > 0.3$ Å, we observe the opposite trend. These strong systems are not less numerous at higher redshift as a result of harsh ionizing conditions in the halos of galaxies. We therefore disfavor the hypothesis that changes in ionzation conditions in the halos of galaxies could drive the observed enhancement in the number of strong Mg II absorbers at redshift $z \sim 2$ compared to $z \sim 0.5$.

The metallicity of the CGM has been best characterized by studies of DLAs and sub-DLAs located in the halos of galaxies, where many metal line transitions are observable, such as Rafelski et al. (2012), Quiret et al. (2016), and Jorgenson et al. (2013). They found a rough trend of decreasing metallicity with increasing redshift dominated by scatter. These high column density systems certainly do not trace all ionized gas in the halos of galaxies as DLAs are predominantly neutral. Using a sample of gravitationally lensed galaxies, it has also been shown that the overall gas phase metallicity of star forming galaxies is 0.35 dex lower at $z \sim 2$ than at $z \sim 0$ (Yuan et al. 2013). In addition, Wotta et al. (2016) and Lehner et al. (2016) examined Lyman Limit Systems (LLS) and found that at $0.1 \leq z \leq 1.1$, the metallicity distribution is bimodal with peaks at $[X/H] \simeq -1.8$ and -0.3. At $z \geq 2$, they found a unimodal distribution with a peak at $[X/H] \simeq -2$. Assuming, then, that over time the overall metallicity of the circumgalactic medium increases, it would not be expected to observe larger quantities of Mg II at $z \sim 2$ compared to $z \sim 0$. In fact, metals should build up over time in the halos of galaxies, producing more Mg II absorption at lower redshift. We can better understand the role of metallicity by again comparing the sample of weak Mg II absorbers to strong Mg II absorbers. The weak systems follow the trend of rising CGM metallicity with time, by having a higher dN/dX at $z \sim 0$ as compared to $z \sim 2$. However, the strongest Mg II systems evolve in an opposite manner to trends in cosmic metallicity, implying that other physical properties drive their evolution. Furthermore, these very high equivalent width systems have the highest column densities, and with these strong systems being more numerous at higher redshifts, they drive the cosmic matter density of Mg II absorbing gas to its highest value at $z \sim 2$. Cosmic metallicity evolution alone, then, cannot explain the slightly enhanced cosmic mass density of Mg II absorbing gas

at $z \sim 2$ as compared to $z \sim 0$.

This leaves us, then, with the most likely conclusion being that galaxies eject more gas into their halos at $z \sim 2$ than at any other time in the form of strong, high equivalent width absorbers. Behroozi et al. (2013) combined galaxy star formation rate measurements from 19 independent studies from 2006 – 2012, spanning redshifts from $0 < z < 8$, to examine evolution in the cosmic star formation rate. They found that galaxies at $z \sim 2$ were forming stars at higher rates than any other time in cosmic history. It follows then that galaxies were ejecting more metal-enriched gas at $z \sim 2$ than at present through supernovae-driven outflows. Under the assumption that these outflows are observable as Mg II absorption systems, they should manifenst themselves in the form of high equivalent width, high column density Mg II absorbers, dense enough to be shielded from the more intense ionizing background at $z \sim 2$, enhanced in metallicity due to their supernovae origins. Therefore, despite competing factors such as a more intense ionizing background and lower overall cosmic metallicity at higher redshifts, we should measure a larger value of $\Omega_{\rm Mg\,II}$ at $z \sim 2$ than at present as a result of galaxy feedback processes ejecting large quantities of Mg II absorbing gas into their halos.

Strong Mg II absorbers still exist at low redshift—their comoving line density does not go to zero at any point in time. However, at low redshifts near the present epoch, the majority of Mg II absorbers are weak, low equivalent width, low column density systems whose properties are likely governed more by metallicity and incident radiation, due to their lower densities disfavoring any self-shielding. These weak absorbers may represent a population of either fragmented outflows, or newly condensed gas in the halos of galaxies (Maller & Bullock 2004). Their eventual fate may be to accrete onto their host galaxy, but this rate of accretion must be small compared to the rate at which the cosmic ionizing background weakens and the cosmic metallicity of the halo increases towards lower redshifts. In other words, the rate of creation of weak Mg II absorbers over time from $z \sim 2$ to the present epoch is greater than the rate of destruction, and this rate of creation may not be tied to an increased quantity of Mg II absorbing gas in the halos of galaxies, but instead an evolution in cosmic properties governing the ionization state of all gas in galactic halos. We must now ask why the weakest systems build up slowly from $z > 2$ to the present epoch, directly opposing the trends observed for the strongest systems. To answer this question, we must understand the innate physical similarities and differences between high equivalent, high column density absorbers and low equivalent width, low column density absorbers.

Studies associated with COS-Halos (Tumlinson et al. 2011) seeking to understand the distribution of metals around galaxies have found the majority of cool, metal absorbing gas lies within the virial radius of galaxies (Peeples et al. 2014). Stern et al. (2016) also found that the mean cool gas density profile around galaxies scales as R^{-1}, with most strong, low ionization metal absorbers existing near the galaxy itself. Further refining these assertions specifically for Mg II, Churchill et al. (2013a) found that the covering fraction of Mg II absorbers falls to 0 at projected distances beyond the virial radius. This means that the Mg II absorbers observed in The Vulture Survey likely lie within the virial radius of a galaxy. The Mg II absorbing gas observed near $z \sim 2$ should eventually fall onto its host galaxy, or stall at large radii and remain a permanent part of the host galaxy halo (Oppenheimer et al. 2010; Ford et al. 2014). What we observe in the form of low redshift Mg II absorbers therefore may not only be the result of outflows near the present epoch, but also the remnants of the most energetic star-forming period in cosmic history.

Perhaps the most clear-cut evidence that many very strong ($W_r^{\lambda 2796} > 1.0$ Å) absorbers have their origins in star formation driven winds comes from the works of Matejek & Simcoe (2012) and Chen et al. (2016). The authors examined their sample of high equivalent width Mg II absorbers spanning redshifts $2 < z < 7$, combined with samples from Nestor et al. (2005) and Prochter et al. (2006) with data below $z < 2$, to relate the Mg II population distribution with the cosmic star formation rate density. Following the methods of Ménard et al. (2011), they convert the Mg II rest frame equivalent widths to a comoving [O II] luminosity density, and from there derive a star formation rate density. When these Mg II-derived star formation rate densities were compared with the mean galaxy specific star formation rates from $0 < z < 7$, they found remarkable agreement. We therefore corroborate their results, finding good agreement between the evolutionary behavior of dN/dX for strong Mg II absorbers and the cosmic star formation rate density. These high equivalent width Mg II systems are preferentially produced by feedback processes associated with star formation.

Referring back to Figure 5(a), we can examine how $\frac{c}{H_o} n_0 \sigma_0$ changes for absorbers of different equivalent widths. Here, we can infer that the physical parameter causing dN/dX to fall between $z \sim 0$ to $z \sim 2$ is the number density of weak Mg II absorbers in galaxy halos (n_0), instead of the absorbing cross-section (σ_0). In Evans et al. (2013), the authors use Cloudy (Ferland et al. 2013) to estimate the size and number densities of clouds giving rise to Mg II absorption. According to these simulations, absorber sizes are roughly an order of magnitude smaller at $z \sim 0$ than they were at $z \sim 2$ for clouds of the same hydrogen density across a wide range of densities. This implies the absorbing cross-section is lower at present than at $z \sim 2$, and, therefore, the number density of weak Mg II absorbers should be the driving factor leading to the enhancement of dN/dX for low equivalent width systems at the present epoch.

Furthermore, Churchill et al. (2013b) discussed how the theoretical cooling radius, the radial distance from the center of a halo at which the initial gas density equals the characteristic density at which gas can cool, may serve as an important factor in determining the observational properties of Mg II absorbers. They found that within the cooling radius, the covering fraction of Mg II absorption increases, and does so most dramatically for absorbers with equivalent widths below $W_r^{\lambda 2796} = 0.3$ Å. At equivalent widths above this level, covering fractions inside and outside the cooling radius are statistically similar. This points toward a possible physical origin for a substantial portion of weak, low equivalent width Mg II absorbers—these clouds cool and condense from collapsing gas clouds within the cooling radius. This gas could have originated from fragmented outflows or infalling material which, over time, met the conditions required to cool enough to be observed as Mg II, instead of a higher, more ionized species.

Given the above considerations, we favor a picture where galaxies, during the most active epoch of star formation in cosmic history, expell large quantities of metal enriched gas into their halos through star formation driven outflows at

$z \sim 2$. These outflows manifest themselves in observations as strong Mg II absorbers. Their destiny will be to eventually either fall back onto the galaxy and enrich the ISM or remain in the halo, subject to the cosmic ionizing background and possible fragmentation. Those absorbers which remain intact and accrete onto the galaxy are lost from observations at lower redshifts, while those which remain at larger radii will likely reach equilibrium with the ionization conditions in the halo. As the intensity of the cosmic ionizing background decreases with time, and more metals are ejected into the halo over time, more of this gas appears as weak Mg II absorption near $z \sim 0$. Many of these weak Mg II absorbers are likely more passive in nature, participating less in the overall baryon cycle in and out of galaxies, subject primarily to the environmental conditions of the CGM.

5. CONCLUSIONS

Using archival data from VLT/UVES and Keck/HIRES, we have undertaken the most complete survey of Mg II absorbers in 602 quasar spectra with high resolution (~ 7 km s^{-1}), allowing for the detection of both strong and weak Mg II absorbsers. Our survey spans absorption redshifts from $0.18 < z < 2.57$, allowing for characterization of the evolution of the distribution of these absorbers across cosmic time. Using our own detection and analysis software, we are able to accurately characterize the equivalent width detection limit, absorption path length, and survey copmleteness to a level allowing for an accurate determination of dN/dz, the equivalent width distribution function, the column density distribution function, and the total cosmic mass density of Mg II absorbers. Our main findings are as follows:

1. We find 1180 intervening Mg II absorption line systems with equivalent widths from 0.003 Å to 8.5 Å, and redshifts spanning $0.14 \leq z \leq 2.64$.

2. We present the distributions of the number of absorbers per unit redshift, dN/dz, and the comoving Mg II line density, dN/dX, as a function of minimum equivalent width threshold and as a function of redshift. We parameterize the evolution in dN/dX specifically with an emperical fit to the distribution in the form of $dN/dX = \frac{c}{H_o} n_0 \sigma_0 (1+z)^{\epsilon}$, showing ϵ increases from $\epsilon = -1.11$ for all absorbers with $W_r^{\lambda 2796} \geq 0.01$ Å to $\epsilon = 0.88$ for absorbers with $W_r^{\lambda 2796} \geq 2$ Å. High equivalent width Mg II absorbers decrease in relative number per absorption path length from $z = 2$ to present, and low equivalent width Mg II absorbers increase in relative number per absorption path length from $z = 2$ to present. We observe no evolution with redshift in absorbers with equivalent widths between $0.2 < W_r^{\lambda 2796} < 1$ Å.

3. We derive a closed form analytic parameterization of dN/dX for all Mg II absorbers. As shown in Equation 10, dN/dX can be expressed as a function of $W_{r,\mathrm{min}}^{\lambda 2796}$ and z. In this parameterization, we also show how the comoving Hubble optical depth, $\frac{c}{H_o} n_0 \sigma_0$, and evolution parameter, ϵ evolve with increasing minimum sample equivalent width (see Figure 5). These form a physical basis for understanding how the comoving line density of Mg II absorbers evolves over cosmic time.

4. The equivalent width distribution function and the column density distribution function for Mg II absorbers are both well fit by a Schecter Function, with a characteristic normalization, faint end slope, and exponential cutoff. Both functions show redshift evolution, specifically in the faint end slope, with this slope becoming shallower for redshifts near $z \sim 2$ as compared to the present epoch. There exist proportionately more high equivalent width, high column density Mg II absorbers near $z \sim 2$ than at present.

5. The cosmic mass density of Mg II absorbing gas, $\Omega_{\mathrm{Mg\,II}}$, increases from $\Omega_{\mathrm{Mg\,II}} \simeq 0.8 \times 10^{-8}$ at $z = 0.5$ to $\Omega_{\mathrm{Mg\,II}} \simeq 1.3 \times 10^{-8}$ at $z \sim 2$.

6. The evolution in dN/dX for the highest equivalent width Mg II absorbers ($W_r^{\lambda 2796} > 1.0$ Å) follows evolutionary trends in the cosmic star formation rate density, which peaks near $z \sim 2$ and falls towards $z \sim 0$. This implies a connection between these very strong systems and star formation driven outflows. Examining other possible factors which could influence the properties of Mg II absorbing gas, such as evolution in the intensity of the cosmic ionizing background and changes in cosmic metallicity, we find that the primary effect driving the evolution of the strongest Mg II absorbers is the quantity of metal enriched gas expelled through star formation driven feedback.

7. We interpret the evolution of low equivalent width Mg II absorbers ($W_r^{\lambda 2796} < 0.3$ Å) as a natural consequence of the evolution in the cosmic ionizing background and the metallicity of galaxy halos. These weaker systems potentially originate in the fragmented remains of star formation driven outflows and lower density gas clouds condensing within the host galaxy's cooling radius. They likely represent a lower density, passive component of the CGM, physically distinct from the strongest Mg II systems.

M.T.M. thanks the Australian Research Council for *Discovery Project* grant DP130100568 which supported this work. C.W.C. thanks the National Science Foundation for the grant AST-1517816, which partially supported this work.

REFERENCES

Bagdonaite, J., Ubachs, W., Murphy, M. T., & Whitmore, J. B. 2014, ApJ, 782, 10
Behroozi, P. S., Wechsler, R. H., & Conroy, C. 2013, ApJ, 770, 57
Bordoloi, R., Lilly, S. J., Kacprzak, G. G., & Churchill, C. W. 2014, ApJ, 784, 108
Bordoloi, R., Lilly, S. J., Knobel, C., et al. 2011, ApJ, 743, 10
Bouché, N., Murphy, M. T., Péroux, C., Csabai, I., & Wild, V. 2006, MNRAS, 371, 495
Charlton, J. C., Mellon, R. R., Rigby, J. R., & Churchill, C. W. 2000, ApJ, 545, 635
Chen, H.-W., Wild, V., Tinker, J. L., et al. 2010, ApJ, 724, L176
Chen, S.-F. S., Simcoe, R. A., Torrey, P., et al. 2016, ArXiv e-prints
Churchill, C. W., Nielsen, N. M., Kacprzak, G. G., & Trujillo-Gomez, S. 2013a, ApJ, 763, L42
Churchill, C. W., Rigby, J. R., Charlton, J. C., & Vogt, S. S. 1999, ApJS, 120, 51
Churchill, C. W., Trujillo-Gomez, S., Nielsen, N. M., & Kacprzak, G. G. 2013b, ApJ, 779, 87
Churchill, C. W., & Vogt, S. S. 2001, AJ, 122, 679
Churchill, C. W., Vogt, S. S., & Charlton, J. C. 2003, AJ, 125, 98
Davidson, R., & MacKinnon, J. G. 2000, Econometric Reviews, 19, 55
Dekker, H., D'Odorico, S., Kaufer, A., Delabre, B., & Kotzlowski, H. 2000, in Proc. SPIE, Vol. 4008, Optical and IR Telescope Instrumentation and Detectors, ed. M. Iye & A. F. Moorwood, 534–545
Evans, J. L., Churchill, C. W., Murphy, M. T., Nielsen, N. M., & Klimek, E. S. 2013, ApJ, 768, 3

Ferland, G. J., Porter, R. L., van Hoof, P. A. M., et al. 2013, Revista Mexicana de Astronomia y Astrofisica, 49, 137
Ford, A. B., Davé, R., Oppenheimer, B. D., et al. 2014, MNRAS, 444, 1260
Ford, A. B., Oppenheimer, B. D., Davé, R., et al. 2013, MNRAS, 432, 89
Gauthier, J.-R., Chen, H.-W., & Tinker, J. L. 2009, ApJ, 702, 50
Haardt, F., & Madau, P. 2012, ApJ, 746, 125
Jorgenson, R. A., Murphy, M. T., & Thompson, R. 2013, MNRAS, 435, 482
Kacprzak, G. G., & Churchill, C. W. 2011, ApJ, 743, L34
Kacprzak, G. G., Churchill, C. W., Evans, J. L., Murphy, M. T., & Steidel, C. C. 2011, MNRAS, 416, 3118
Kacprzak, G. G., Churchill, C. W., & Nielsen, N. M. 2012, ApJ, 760, L7
King, J. A., Webb, J. K., Murphy, M. T., et al. 2012, MNRAS, 422, 3370
Kulkarni, V. P., & Fall, S. M. 2002, ApJ, 580, 732
Kulkarni, V. P., Fall, S. M., Lauroesch, J. T., et al. 2005, ApJ, 618, 68
Kulkarni, V. P., Khare, P., Péroux, C., et al. 2007, ApJ, 661, 88
Lanzetta, K. M., Turnshek, D. A., & Wolfe, A. M. 1987, ApJ, 322, 739
Lehner, N., O'Meara, J. M., Howk, J. C., Prochaska, J. X., & Fumagalli, M. 2016, ArXiv e-prints
Lovegrove, E., & Simcoe, R. A. 2011, ApJ, 740, 30
Lundgren, B. F., Brunner, R. J., York, D. G., et al. 2009, ApJ, 698, 819
Maller, A. H., & Bullock, J. S. 2004, MNRAS, 355, 694
Martin, C. L., & Bouché, N. 2009, ApJ, 703, 1394
Matejek, M. S., & Simcoe, R. A. 2012, ApJ, 761, 112
Matejek, M. S., Simcoe, R. A., Cooksey, K. L., & Seyffert, E. N. 2013, ApJ, 764, 9
Ménard, B., & Chelouche, D. 2009, MNRAS, 393, 808
Ménard, B., Wild, V., Nestor, D., et al. 2011, MNRAS, 417, 801
Murphy, M. T. 2016, UVES_popler: POst PipeLine Echelle Reduction software, doi:10.5281/zenodo.44765
—. in prep, MNRAS
Murphy, M. T., Malec, A. L., & Prochaska, J. X. 2016, MNRAS, 461, 2461
Narayanan, A., Charlton, J. C., Masiero, J. R., & Lynch, R. 2005, ApJ, 632, 92
Narayanan, A., Misawa, T., Charlton, J. C., & Kim, T.-S. 2007, ApJ, 660, 1093
Nestor, D. B., Johnson, B. D., Wild, V., et al. 2011, MNRAS, 412, 1559
Nestor, D. B., Turnshek, D. A., & Rao, S. M. 2005, ApJ, 628, 637
Nielsen, N. M., Churchill, C. W., & Kacprzak, G. G. 2013a, ApJ, 776, 115
Nielsen, N. M., Churchill, C. W., Kacprzak, G. G., & Murphy, M. T. 2013b, ApJ, 776, 114
Nielsen, N. M., Churchill, C. W., Kacprzak, G. G., Murphy, M. T., & Evans, J. L. 2015, ApJ, 812, 83
—. 2016, ApJ, 818, 171
Noterdaeme, P., Srianand, R., & Mohan, V. 2010, MNRAS, 403, 906
O'Meara, J. M., Lehner, N., Howk, J. C., et al. 2015, AJ, 150, 111
Oppenheimer, B. D., Davé, R., Kereš, D., et al. 2010, MNRAS, 406, 2325
Peeples, M. S., Werk, J. K., Tumlinson, J., et al. 2014, ApJ, 786, 54
Planck Collaboration, Ade, P. A. R., Aghanim, N., et al. 2016, A&A, 594, A13
Prochaska, J. X., Gawiser, E., Wolfe, A. M., Castro, S., & Djorgovski, S. G. 2003, ApJ, 595, L9
Prochter, G. E., Prochaska, J. X., & Burles, S. M. 2006, ApJ, 639, 766
Quiret, S., Péroux, C., Zafar, T., et al. 2016, MNRAS
Rafelski, M., Wolfe, A. M., Prochaska, J. X., Neeleman, M., & Mendez, A. J. 2012, ApJ, 755, 89
Rigby, J. R., Charlton, J. C., & Churchill, C. W. 2002, ApJ, 565, 743
Rubin, K. H. R., Weiner, B. J., Koo, D. C., et al. 2010, ApJ, 719, 1503
Sargent, W. L. W., Steidel, C. C., & Boksenberg, A. 1988, ApJ, 334, 22
Sharma, M., & Nath, B. B. 2013, ApJ, 763, 17
Shattow, G. M., Croton, D. J., & Bibiano, A. 2015, MNRAS, 450, 2306
Steidel, C. C., & Sargent, W. L. W. 1992, ApJS, 80, 1
Stern, J., Hennawi, J. F., Prochaska, J. X., & Werk, J. K. 2016, ArXiv e-prints
Stewart, K. R., Kaufmann, T., Bullock, J. S., et al. 2011, ApJ, 738, 39
Tremonti, C. A., Moustakas, J., & Diamond-Stanic, A. M. 2007, ApJ, 663, L77
Tumlinson, J., Thom, C., Werk, J. K., et al. 2011, Science, 334, 948
Tytler, D., Boksenberg, A., Sargent, W. L. W., Young, P., & Kunth, D. 1987, ApJS, 64, 667
Vogt, S. S., Allen, S. L., Bigelow, B. C., et al. 1994, in Proc. SPIE, Vol. 2198, Instrumentation in Astronomy VIII, ed. D. L. Crawford & E. R. Craine, 362
Weiner, B. J., Coil, A. L., Prochaska, J. X., et al. 2009, ApJ, 692, 187
Wotta, C. B., Lehner, N., Howk, J. C., O'Meara, J. M., & Prochaska, J. X. 2016, ApJ, 831, 95
Yuan, T.-T., Kewley, L. J., & Richard, J. 2013, ApJ, 763, 9
Zhu, B. G., Comparat, J., Kneib, J.-P., et al. 2015, ApJ, 815, 48
Zhu, G., & Ménard, B. 2013, ApJ, 770, 130
Zibetti, S., Ménard, B., Nestor, D. B., et al. 2007, ApJ, 658, 161